16.4 A One-Stage Bidirectional Rectifier with Pre-Charge-Based MPPT for Triboelectric Energy Harvesting with 93% MPPT Efficiency and 8.86× Power Enhancement

Wenyu Peng, Jida Peng, Willem van Driel, Guoqi Zhang, Sijun Du

Delft University of Technology, Delft, The Netherlands

Abstract

This work proposes a one-stage bidirectional rectifier with a pre-charge voltage (V_{PC}) based perturb-and-observe (P&O) maximum power point tracking (MPPT) algorithm for triboelectric energy harvesting. The proposed V_{PC}-based MPPT dynamically locates the true MPP while accounting for circuit non-idealities, using a simplified implementation compared to conventional P&O methods. Consequently, it achieves 93% MPPT efficiency and 8.86× energy enhancement compared to the full-bridge rectifier.

With the growth of Internet-of-Things (IoT) and edge computing, wireless sensor networks (WSNs) are widely deployed at the end where battery life is critical. Energy harvesting (EH) has been a promising solution to eliminate batteries or extend the battery life. Among various EH techniques, triboelectric nanogenerators (TENGs) harvest irregular mechanical energy but produce a high-voltage (HV) AC output (V_T) with a time-varying intrinsic capacitance (C_T) [1,2], as shown in Fig.16.4.1 (top), thus requiring specialized rectifiers to deliver usable sub-5V DC power. Prior interfaces such as bias-flip (BF) [3-7] and electrostatic charge boosting (ECB) [8] rely on an HV storage capacitor (C_{REC}) and a separate DC-DC stage, incurring leakage, slow startup, and cascaded loss.

This work proposes a one-stage bidirectional rectifier with a pre-charge voltage (V_{PC})-based perturb-and-observe (P&O) maximum power point tracking (MPPT) algorithm (Fig. 16.4.1 bottom). The one-stage topology removes the HV-capacitor leakage and directly steps the TENG voltage down to sub-5 V. The proposed V_{PC}-based MPPT dynamically locates the true MPP while accounting for circuit non-idealities, using a simplified implementation compared to conventional P&O methods. Within each kinetic period (T_k), the rectifier alternates between harvest (blue) and invest (red) phases. In the positive half-cycle (Φ_P), phase I starts, where V_T is pre-charged from V_{OUT} to a given pre-charge voltage, $V_{PC,p}$. Phase II maintains V_T near the harvesting voltage (V_{HAR}) (typically the process limit for high power, e.g., 65V) using multi-shot conversions to extract power form the TENG to V_{OUT}. Phase III extracts the remaining energy from C_T to prevent self-discharge. The negative half-cycle (Φ_N) includes phases IV – VI, which mirror phases I – III but operate with reversed polarity and a separate pre-charge voltage $V_{PC,n}$. Among these six phases, $V_{PC,p}$ and $V_{PC,n}$ determine the energy invested from V_{OUT} to the TENG. Since Φ_P typically delivers much higher energy than Φ_N, the MPPT algorithm focuses on tracking the optimal $V_{PC,p}$ (i.e., $V_{PC,MPP}$), while the $V_{PC,n}$ is externally set to reduce system complexity.

The power stage of the proposed rectifier (Fig. 16.4.2) employs seven on-chip 65-V n-type LDMOS transistors ($S_{1\sim7}$) to integrate both rectification and bidirectional power conversion. Node V_X, connected to V_{OUT} via an inductor, exhibits a tens-of-pF parasitic capacitance (C_{para}) from the HV switches, inductor, and packaging, which complicates precise MPP tracking. Figure 16.4.2 (bottom) illustrates the waveforms of V_T, V_X, and the inductor current (I_L) across phases I – III. The corresponding operation steps ($OP_\#$) are shown in Fig. 16.4.2 (top-right). In phase I, V_T is pre-charged to $V_{PC,p}$ via two operations: OP_1, which charges the inductor, and OP_{3P}, which transfers energy to the TENG. In phase II, energy extraction begins when V_T reaches 65V. To minimize conduction loss and reduce the quality factor requirements of the inductor, multiple low-current energy conversion shots are used [9]. This allows the use of a compact 470μH inductor. In each shot, C_{para} is first charged through LC resonance by OP_1 and OP_{3P} to suppress the hard-charging loss and V_T ripple caused by C_{para}, The OP_1 duration is adaptively tuned to avoid overcharging. Once V_X peaks during OP_{3P}, OP_{2P} is triggered to let the TENG briefly charge the inductor. A short dead time during OP_0 follows, allowing residual C_{para} energy to enter the inductor. When V_X falls below 0V, OP_1 resumes to transfer I_L efficiently to V_{OUT}. Phase II continues until V_T starts decreasing due to the polarity change of I_T, marking the start of phase III, which uses the same operation sequence as phase II but with different durations. As V_T declines, the duration of OP_{2P} is extended to maintain energy delivery. By the end of phase III, V_T is fully discharged to 0V. Phases IV – VI repeat the same operation pattern during Φ_N with opposite polarities and the replacement of OP_{2P} and OP_{3P} with OP_{2N} and OP_{3N}.

Figure 16.4.3 (left) illustrates the mechanism and implementation of the proposed V_{PC}-based MPPT algorithm. In each cycle, the system must determine an optimal $V_{PC,p}$ that maximizes the net output energy. To do so, it evaluates the energy balance during phase I (investment) and phase II (harvesting) by analyzing each power conversion shot. Each shot is composed of two time periods: the pre-charge period (T_{PC}) when V_{OUT} charges the inductor, and the harvesting period (T_{HAR}) when energy is delivered from the inductor to V_{OUT}. As I_L rises linearly (slope = V_{OUT}/L), the net transferred energy per shot is proportional to $T_{CONV}^2 - T_{PC}^2$, or equivalently, $(T_{CONV} - T_{PC})(T_{CONV} + T_{PC})$. To simplify computation, the term $T_{CONV} - T_{PC}$ is kept constant across all shots, enabling linear rescaling of the energy input and output using only time measurements. Based on this, the system estimates the invested energy $E_{I,k}$ and harvested energy $E_{II,k}$ during the k^{th} T_k. Then, in the $(k+1)^{th}$ cycle, the MPPT controller perturbs $V_{PC,p}$ by injecting two additional pre-charging shots in phase I (i.e., $M_{k+1} = M_k + 2$). The resulting change in harvested energy, $\Delta E = E_{II,k+1} - E_{II,k}$, reflects the system's position relative to the MPP: if ΔE exceeds 150% of the extra injected energy, it implies that $V_{PC,p}$ is below the optimum, and the next perturbation increases to +3 shots; otherwise, if ΔE is smaller, the perturbation is reversed (–3 shots) to reduce $V_{PC,p}$, and in this case, the energy comparison step is skipped to save computation. This pre-charge-based P&O method offers real-time tracking with low hardware complexity, requiring only simple time counters and avoiding multipliers or analog computation.

Figure 16.4.3 (right) shows the architecture of the proposed system. The LDMOS switches in the power stage are driven by level shifters and bootstrap gate drivers. A peak voltage detector (PVD) connected to V_P identifies the transition from positive to negative semi-cycle (Φ_P to Φ_N), thereby synchronizing the control phases. At V_N, a HV sample and hold (S&H) block and a 6-bit successive approximation register (SAR) ADC are used to define $V_{PC,n}$. However, since the inherent capacitance C_T increases during Φ_N and the available harvested energy is very limited, implementing dynamic MPPT for $V_{PC,n}$ is not cost-effective. To reduce system complexity and power overhead, $V_{PC,n}$ is set externally and kept constant. The system also incorporates voltage sensors at both V_P and V_N to monitor V_T. Once V_T reaches 65V, these sensors trigger energy harvesting actions to regulate V_T and protect the circuit. V_X is connected to a second PVD, a zero current detector, and a hard-charging detector. These auxiliary sensors track inductor and capacitor dynamics in real-time and coordinate the switching between internal operations such as OP_1–OP_3.

The proposed chip is fabricated in a 0.18μm BCD process. The TENG used for validation is in-house fabricated, featuring copper-nickel tape electrodes, and triboelectric layers composed of nylon and PTFE films, as shown in Fig. 16.4.4 (top-left). This device achieves an open-circuit voltage exceeding 70V during Φ_N ($V_{OC\text{-}}$), with a C_T swing from approximately 50-to-500pF. Figure 16.4.4 illustrates the measured waveforms when the TENG operates with a 45Hz kinetic excitation. Each operational cycle is divided into six distinct phases (I – VI), each further split into multiple fine-grained energy conversion shots to reduce conduction loss. In phase I, the number of pre-charging shots is dynamically determined by the V_{PC}-based MPPT algorithm. As shown in Fig. 16.4.4 (top-right), $V_{PC,p}$ is perturbed and adjusted across cycles, enabling real-time tracking of net energy gain under different pre-charge voltages. During phase II, once V_P reaches 65V, the system initiates the controlled energy extraction via multi-shot conversions from the TENG to V_{OUT}. The averaged voltage drop during this phase is around 6V, allowing V_T to remain near V_{HAR} for efficient harvesting. At the end of Φ_P, when V_P begins to fall, phase III is initiated to complete charge extraction from C_T, driving V_P toward 0V using a series of small shots. The Φ_N half cycle mirrors this behavior: in phase IV, V_N is pre-charged to ~10V (with $V_{PC,n}$, set manually). In phase V, V_N may reach up to 65V due to the high $V_{OC\text{-}}$, prompting the system to apply several power conversion shots to cap V_N under 65V. In phase VI, the system fully extracts the remaining energy to V_{OUT}. More shots are required here than in phase III, due to the larger C_T during this interval. Finally, Fig. 16.4.5 (top-left) shows the detailed waveforms of V_P, V_N, and V_X during a single energy conversion shot. OP_{3P} charges the parasitic capacitor at V_X up to ~55V via soft charging, effectively reducing the hard-charging loss.

Figure 16.4.5 (top-right) presents the energy-extraction performance of the proposed rectifier. Leveraging the high open-circuit voltage of the in-house TENG, the system achieves maximum harvested energy when V_{HAR} is set to 65V, reaching a peak extracted power of 101μW. This corresponds to an 8.86× improvement over an ideal full-bridge rectifier (FBR), validating the effectiveness of the proposed synchronized harvesting strategy and one-stage architecture. The power conversion efficiency (PCE) is shown in Fig. 16.4.5 (bottom-left), which shows small variations across V_{OUT}, and a peak efficiency of 60.3% at V_{OUT} = 4.7V, demonstrating robust operation under various load conditions. Figure 16.4.5 (bottom-right) shows the V_{PC}-based MPPT performance. The maximum power output is measured when $V_{PC,p}$ is equal to 16V. When the MPPT algorithm is activated, $V_{PC,p}$ is perturbed between 10V and 25V, resulting in a measured extracted power of 93.8μW. Therefore, the MPPT efficiency is calculated as 93%, showing that the proposed V_{PC}-based MPPT algorithm effectively optimizes the energy extraction from the triboelectric energy harvesting system. The comparison table is presented in Fig. 16.4.6. This work exhibits a one-stage bidirectional rectifier for triboelectric energy harvesting. Compared with other works, it requires zero HV off-chip capacitors. Moreover, a novel V_{PC}-based MPPT algorithm is proposed, which

2026 IEEE International Solid-State Circuits Conference (ISSCC) | 979-8-3315-8936-3/26/$31.00 ©2026 IEEE | DOI: 10.1109/ISSCC49663.2026.11408962

achieves systematic MPPT in triboelectric energy harvesting and a high tracking efficiency of 93%. Lastly, the proposed system improves the power output by 8.86×, indicating a high energy extraction efficiency. Figure 16.4.7 shows the chip micrograph.

References:

[1] Y. Zhou, P. Zhang, J. Li, and X. Mao, "Recent progress of triboelectric nanogenerator-based power management and information processing circuit," *Materials Today Sustainability,* vol. 23, p. 100426, 2023/09/01/ 2023. https://doi.org/10.1016/j.mtsust.2023.100426

[2] W. Peng and S. Du, "The Advances in Conversion Techniques in Triboelectric Energy Harvesting: A Review," in *IEEE Transactions on Circuits and Systems I: Regular Papers*, vol. 70, no. 7, pp. 3049-3062, July 2023. https://doi.org/10.1109/TCSI.2023.3261780

[3] I. Kara, M. Becermis, M. A. -A. Kamar, M. Aktan, H. Dogan and S. Mutlu, "A 70-to-2 V Triboelectric Energy Harvesting System Utilizing Parallel-SSHI Rectifier and DC-DC Converters," in *IEEE Transactions on Circuits and Systems I: Regular Papers*, vol. 68, no. 1, pp. 210-223, Jan. 2021. https://doi.org/10.1109/TCSI.2020.3025468

[4] J. Lee, S. -H. Lee, G. -G. Kang, J. -H. Kim, G. -H. Cho and H. -S. Kim, "A 130V Triboelectric Energy-Harvesting Interface in .18\mu\mathrm{m}$ BCD with Scalable Multi-Chip-Stacked Bias-Flip and Daisy-Chained Synchronous Signaling Technique," *2022 IEEE International Solid-State Circuits Conference (ISSCC)*, San Francisco, CA, USA, 2022, pp. 474-476. https://doi.org/10.1109/ISSCC42614.2022.9731605

[5] S. -H. Lee, Y. -W. Jeong, S. -J. Park and S. -U. Shin, "A Rectifier-Reusing Bias-Flip Energy Harvesting Interface Circuit With Adaptively Reconfigurable SC Converter for Wind-Driven Triboelectric Nanogenerator," in *IEEE Transactions on Industrial Electronics*, vol. 70, no. 8, pp. 8022-8031, Aug. 2023. https://doi.org/10.1109/TIE.2022.3220848

[6] W. Peng, X. Yue, W. van Driel, G. Zhang and S. Du, "A 70-V Fully Integrated Dual-SSHC Rectifier for Triboelectric Energy Harvesting with Full-Digital Duty-Cycle-Based MPPT Achieving 598% Power Extraction Enhancement," *2024 IEEE Custom Integrated Circuits Conference (CICC)*, Denver, CO, USA, 2024, pp. 1-2. https://doi.org/10.1109/CICC60959.2024.10529024

[7] W. Jung, H. -M. Lee and H. -P. Le, "A Reconfigurable Multi-Level AC-DC/DC-DC Ocean Energy Harvester IC Achieving 77.7% End-to-End Power Efficiency for Triboelectric Nanogenerators," *2025 Symposium on VLSI Technology and Circuits (VLSI Technology and Circuits)*, Kyoto, Japan, 2025, pp. 1-3. https://doi.org/10.23919/VLSITechnologyandCir65189.2025.11074895

[8] W. Peng, X. Yue, L. Pakula and S. Du, "A Capacitor-Based Bias-Flip Rectifier with Electrostatic Charge Boosting for Triboelectric Energy Harvesting Achieving Auto-MPPT at Breakdown Voltage and 14× Power Extraction Improvement," *2024 IEEE International Solid-State Circuits Conference (ISSCC)*, San Francisco, CA, USA, 2024, pp. 516-518. https://doi.org/10.1109/ISSCC49657.2024.10454538

[9] Y. -W. Jeong, S. -J. Lee, J. -H. Kim, M. -J. Cho, H. -S. Kim and S. -U. Shin, "A Scalable N-Step Equal Split SSHI Piezoelectric Energy Harvesting Circuit Achieving 1170% Power Extraction Improvement and 22nA Quiescent Current with a 1μH–to–10μH Low Q Inductor," *2023 IEEE International Solid-State Circuits Conference (ISSCC)*, San Francisco, CA, USA, 2023, pp. 438-440. https://doi.org/10.1109/ISSCC42615.2023.10067389

[10] I. Park, J. Maeng, M. Shim, J. Jeong and C. Kim, "A High-Voltage Dual-Input Buck Converter Achieving 52.9% Maximum End-to-End Efficiency for Triboelectric Energy-Harvesting Applications," in *IEEE Journal of Solid-State Circuits*, vol. 55, no. 5, pp. 1324-1336, May 2020. https://doi.org/10.1109/JSSC.2019.2942370

[11] J. Maeng, I. Park, M. Shim, J. Jeong and C. Kim, "A High-Voltage Dual-Input Buck Converter With Bidirectional Inductor Current for Triboelectric Energy-Harvesting Applications," in *IEEE Journal of Solid-State Circuits*, vol. 56, no. 2, pp. 541-553, Feb. 2021. https://doi.org/10.1109/JSSC.2020.3012991

[12] S. -Y. Moon, A. Shafique, S. C. Chandrarathna and J. -W. Lee, "A High-Voltage PMIC Using an Efficient Perturb and Observe Technique for Energy Harvesting of Triboelectric Nanogenerators," in *IEEE Transactions on Power Electronics*, vol. 40, no. 2, pp. 3225-3239, Feb. 2025. https://doi.org/10.1109/TPEL.2024.3484455

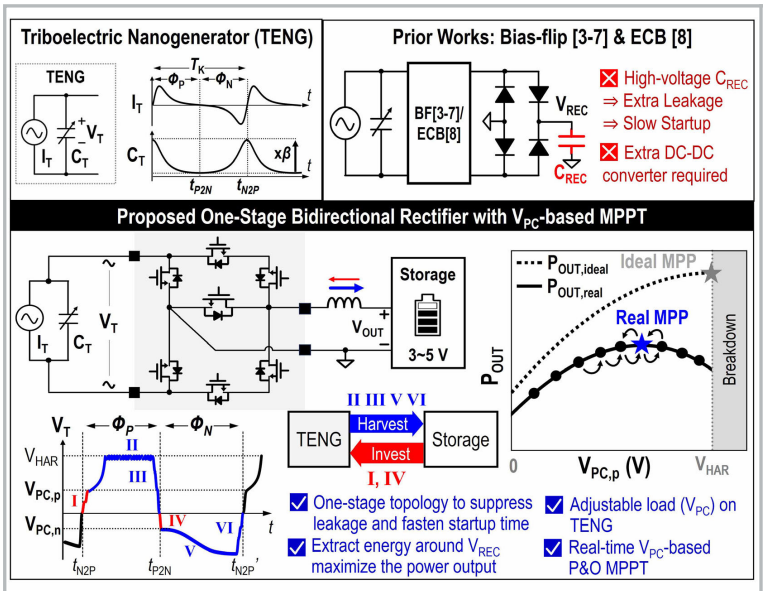

Figure 16.4.1: Conventional rectifiers (top); The proposed one-stage bidirectional rectifier with V_{PC}-based MPPT (bottom).

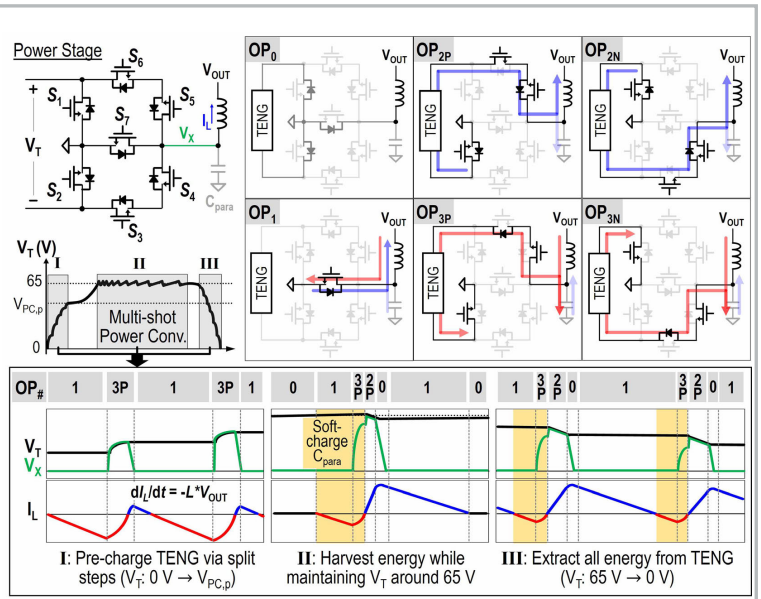

Figure 16.4.2: The operations in each shot in energy harvesting and investing phases.

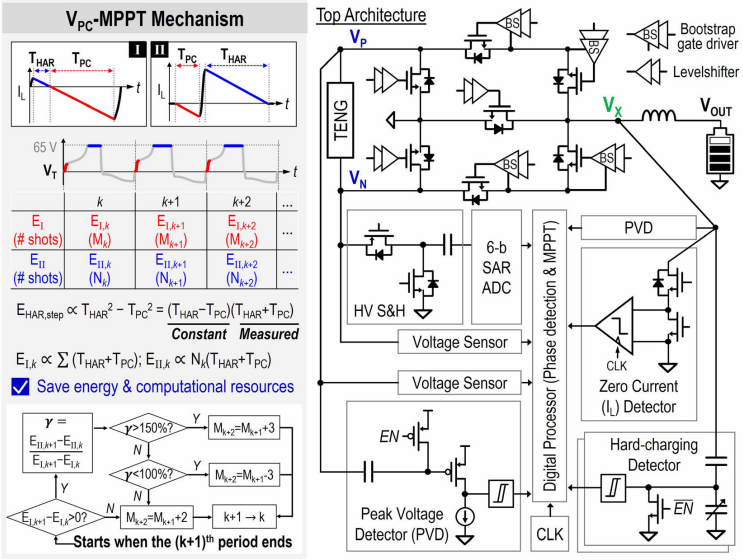

Figure 16.4.3: V_{PC}-MPPT algorithm and logical workflow (left); Top architecture of the proposed energy harvesting system (right).

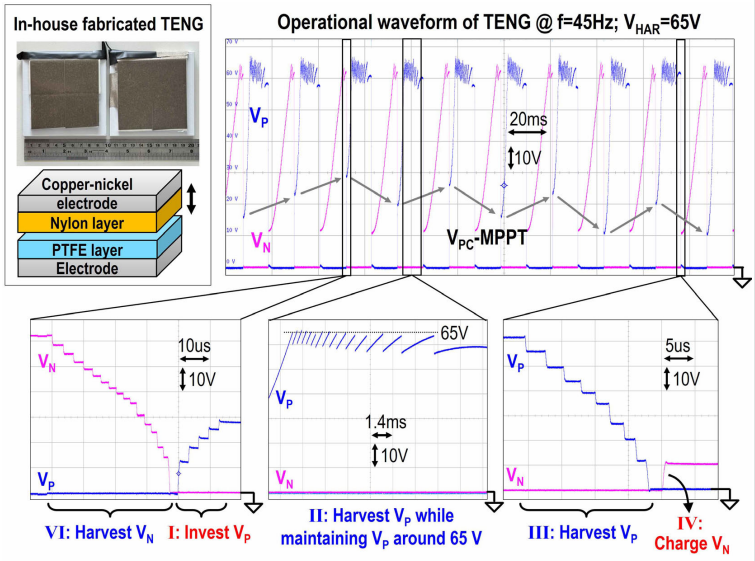

Figure 16.4.4: The structure of TENG (top-left); The measured transient waveform of the proposed rectifier.

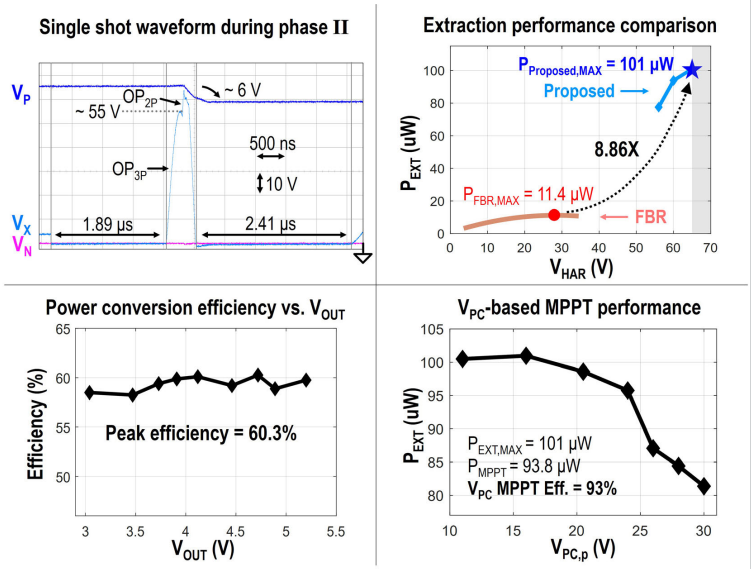

Figure 16.4.5: The measured waveform of a harvesting shot @ phase II (left-top); The measured energy extraction and MPPT performance.

	JSSC'20 [10]	JSSC'21 [11]	ISSCC'22 [4]	ISSCC'24 [8]	CICC'24 [6]	TPE'25 [12]	VLSI'25 [7]	This work
Process	0.18-µm BCD	0.18-µm BCD	0.18-µm BCD	0.18-µm BCD	0.18-µm BCD	0.18-µm BCD	0.18-µm BCD	0.18-µm BCD
Transducer	TENG	TENG	Wind-TENG	TENG	TENG	TENG	TENG	TENG
Inherent Capacitance	Varying	Varying	Constant	Varying	Varying	Varying	Constant	Varying
Frequency (Hz)	20-50	40-55	250	150	70	5	2-50	7-80
Topology	Dual-Output FBR + Dual-Input Buck	Dual-Output FBR + Dual-Input Buck	MCS-BF + SC DC-DC Converter	ECB + Buck	D-SSHC + Buck	FBR + Buck	Multi-level BF + Dual-Input Three-Level Buck	One-Stage Bidirectional Rectifier
Max. Input Voltage (V)	70	70	130/195	70	70	70	70	65
HV (>5V) Capacitors	2	2	2/3	1	1	1	3	0
V_{REC}-MPPT	FOCV	FOCV	N/A	Auto-MPPT @Breakdown Voltage	DCB	P&O	N/A	N/A
V_{PC}-MPPT	N/A	N/A	N/A	N/A	N/A	N/A	N/A	P&O
Peak PCE (%)	51.1	84.7	70.7*	N/A	N/A	85.3	83.7	60.3
Chip area (mm²)	2.03	2.34	4.16(main)/ 1.77(follower)	4.34	2.47	2.75	3.5	1
External Inductor	1 mH	10 mH	10 mH	1 µH	1 µH	20 mH	1 mH	470 µH
Peak Output Power (µW)	20.7	7.2	1211	127.6	85.4	153.5	2008	101
V_{PC}-MPPT Eff. (%)	N/A	N/A	N/A	N/A	N/A	N/A	N/A	93
P_{EXT}/P_{FBR}	N/A	N/A	3.14×	14.0×	5.98×	N/A	6.63×	8.86×

* End-to-end efficiency

Figure 16.4.6: The comparison table between the proposed work and the state-of-the-art.

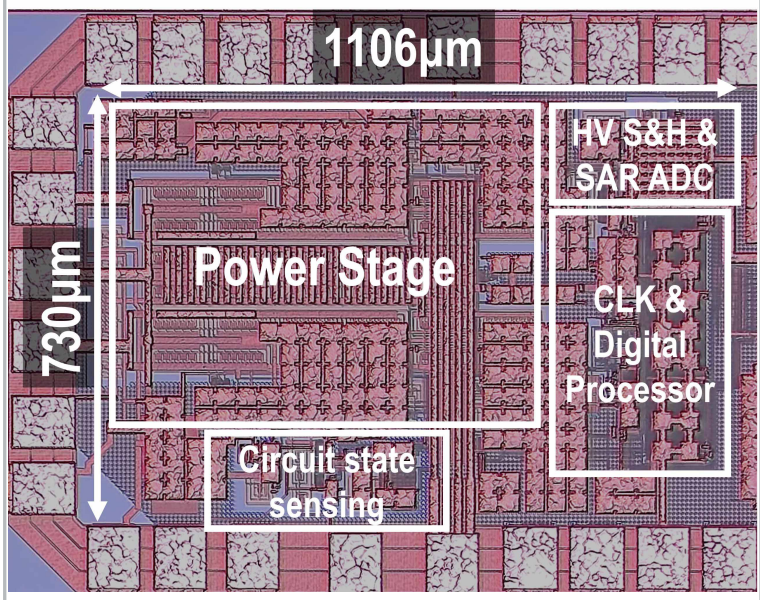

Figure 16.4.7: Chip micrograph.

979-8-3315-8936-3/26/$31.00 ©2026 IEEE